Chemical Science

ROYAL SOCIETY OF CHEMISTRY

EDGE ARTICLE

View Article Online
View Journal | View Issue

Cite this: *Chem. Sci.*, 2024, **15**, 15480

All publication charges for this article have been paid for by the Royal Society of Chemistry

Boosting circularly polarized luminescence by optimizing off-centering octahedral distortion in zero-dimensional hybrid indium-antimony halides†

Yulian Liu, Yi Wei, Zhishan Luo, Bin Xu, Meiying He, Peibin Hong, Chen Li and Zewei Quan *

Received 3rd July 2024
Accepted 24th August 2024

DOI: 10.1039/d4sc04399e

rsc.li/chemical-science

Chiral zero-dimensional hybrid metal halides (0D HMHs) are being extensively studied as they can directly generate circularly polarized luminescence (CPL) with high photoluminescence quantum yields (PLQYs), yet improving their luminescence dissymmetry factor (g_{lum}) remains a challenge. This study proposes a general strategy to boost the g_{lum} value of chiral 0D HMHs by optimizing the off-centering distortion ($\mathcal{D}$) of inorganic octahedra. Accordingly, $(R/S\text{-MBA})_2(2MA)In_{0.95}Sb_{0.05}Cl_6$ (MBA = α-methylbenzylammonium, 2MA = dimethylamine) and $(R/S\text{-MBA})_2(3MA)In_{0.95}Sb_{0.05}Cl_6$ (3MA = trimethylamine) with near-unity PLQYs are accordingly synthesized. With increasing the $\mathcal{D}$ from 0.012 to 0.020, the $|g_{lum}|$ is accordingly increased from 7.8×10^{-3} to 2.0×10^{-2}. Notably, the $|g_{lum}|$ can be further boosted to an impressive value of 3.8×10^{-2} while maintaining near-unity PLQYs by continuously increasing the $\mathcal{D}$. Experimental results reveal that the choice of achiral ligands and varied Sb^{3+} dopant concentrations can modulate the distribution and strength of hydrogen bonds around indium-antimony halogen octahedra, respectively, thus regulating the $\mathcal{D}$ parameter of octahedra in 0D hybrid metal halides. Additionally, light-emitting diodes with a polarization of 1.6% are fabricated. This work sheds light on the relationship between the distortion of inorganic octahedra and the g_{lum} value.

Introduction

Circularly polarized luminescence (CPL) has attracted tremendous research interest due to its potential applications in a wide variety of fields such as three-dimensional displays, quantum computing and optical information storage.[1–6] Novel and efficient devices to generate and detect CPL are thus of great importance. In conventional polarized emitters, additional optical elements such as a linear polarizer and a quarter waveplate are included to obtain polarization control. Although efficient polarization control is realized, it hinders their miniaturization and applicability in integration circuits. In this aspect, chiral hybrid metal halides (HMHs) that combine tunable chirality of organic ligands with excellent optical properties of inorganic units can be used to directly detect and generate circularly polarized light. Since the first report of chiral HMHs, significant progress has been made, and a series of chiral HMHs with obvious CPL signals are successfully synthesized.[7–15] Both high photoluminescence quantum yield (PLQY) and large luminescence dissymmetry factor (g_{lum}) values are essential to technical applications of CPL-active materials. However, it is still challenging to achieve chiral HMHs with simultaneously high PLQYs and large g_{lum} values.[16]

Particularly, zero-dimensional (0D) HMHs, in which inorganic polyhedra are fully separated by organic ligands, usually exhibit tunable emissions with high PLQYs.[17–19] Typically, alloying at the In–Sb site is a common strategy to increase the PLQYs of 0D HMHs and also provides a means to modulate the distortion of metal halogen octahedra, thereby improving the g_{lum} values. Besides, low-dimensional chiral HMHs should exhibit a higher degree of chirality as a result of strong intermolecular interactions induced by the greater percentage of chiral ligands.[20] Chiral 0D HMHs are thus expected to be a class of high performance CPL-active materials with both high PLQYs and large g_{lum} values. It has been recently demonstrated that high PLQYs can be readily achieved in chiral 0D HMHs.[21–25] Nevertheless, the g_{lum} values of reported chiral 0D HMHs are relatively low, most of which are in the magnitude of 10^{-3}.[14,23,26] Significant effort has been devoted to enhancing the g_{lum} values of chiral HMHs and understanding the chirality induction mechanism.[27–30] It is found that the asymmetric hydrogen bonds between organic ligands and inorganic frameworks in two-dimensional (2D) HMHs can enhance their g_{lum} values.[31,32] Moreover, the chiroptical activity of chiral 2D hybrid perovskites is revealed to originate from the symmetry-breaking helical distortion of the inorganic lattice induced by the asymmetric

Department of Chemistry, Academy for Advanced Interdisciplinary Studies, Southern University of Science and Technology, China. E-mail: quanzw@sustech.edu.cn

† Electronic supplementary information (ESI) available. CCDC 2344292–2344296. For ESI and crystallographic data in CIF or other electronic format see DOI: https://doi.org/10.1039/d4sc04399e

hydrogen bonding interactions with the inorganic lattice.[33,34] Similar phenomena are recently reported in chiral 0D HMHs. The chiroptical activity of chiral 0D lead-tin bromide hybrids is attributed to the asymmetric polyhedra induced by hydrogen bonds.[22] By modulating the hydrogen bonding interactions between organic ligands and inorganic units, enhanced CPL performance with large g_{lum} values of $\pm 1.0 \times 10^{-2}$ and near-unity PLQY is achieved in a series of chiral indium-antimony hybrids.[25] Right now, the g_{lum} values of chiral 0D HMHs need to be further improved to meet the practical applications of chiral HMHs as chiroptical devices.[10]

In this work, the g_{lum} values of chiral 0D HMHs are significantly improved based on a general strategy, that is, optimizing the off-centering distortion of inorganic octahedra by modulating the strength and distribution of hydrogen bonds around indium-antimony halogen octahedra therein. Five pairs of enantiomorphic $(R/S\text{-MBA})_2(2MA)In_{0.95}Sb_{0.05}Cl_6$ (R/S-1) (MBA = α-methylbenzylammonium, 2MA = dimethylamine) and $(R/S\text{-MBA})_2(3MA)In_{0.95}Sb_{0.05}Cl_6$ (R/S-2) (3MA = trimethylamine), $(R/S\text{-MBA})_2(3MA)In_{0.79}Sb_{0.21}Cl_6$ (R/S-2A), $(R/S\text{-MBA})_2(3MA)In_{0.72}Sb_{0.28}Cl_6$ (R/S–2B) and $(R/S\text{-MBA})_2(3MA)In_{0.59}Sb_{0.41}Cl_6$ (R/S-2C) are synthesized, and all of them exhibit near-unity PLQYs. With adopting different achiral ligands and modifying Sb^{3+} dopant concentrations, the off-centering distortion of inorganic octahedra is continuously increased from 0.012 to 0.047 and the $|g_{abs}|/|g_{lum}|$ is increased from $0.16 \times 10^{-3}/7.8 \times 10^{-3}$ to $1.25 \times 10^{-3}/3.8 \times 10^{-2}$, indicating the crucial role of large off-centering distortion in achieving a high $|g_{abs}|/|g_{lum}|$ value. Moreover, the highest g_{lum} value of $\pm 3.8 \times 10^{-2}$ and near-unity PLQY in R/S-2C outperform those of currently reported chiral HMHs. Combined crystal structure and photophysical studies demonstrate that the distribution and strength of hydrogen bonds can be delicately modified to increase the off-centering distortions of inorganic octahedra. With R-2C as the phosphor, light-emitting diodes with a polarization of 1.6% at room temperature are fabricated, demonstrating their potential as CPL light sources in three-dimensional displays and quantum computing.

Results and discussion

In this work, common chiral R/S-methylbenzylamine (R/S-MBA) ligands are selected as chiral inducers.[20,35] Achiral ligands with different sizes and steric hindrance including dimethylamine hydrochloride (2MACl) and trimethylamine hydrochloride (3MACl) are integrated into chiral HMHs to modulate the hydrogen bonds with inorganic octahedra. $(R/S\text{-MBA})_2(2MA)In_{0.95}Sb_{0.05}Cl_6$ (R/S-1) are synthesized by cooling the aqueous HCl solution of stoichiometric amounts of R/S-MBA, 2MACl, $InCl_3$ and $SbCl_3$. $(R/S\text{-MBA})_2(3MA)In_{0.95}Sb_{0.05}Cl_6$ (R/S-2) are obtained through a similar procedure to R/S-1, except that the achiral ligands are replaced with 3MACl. The synthetic details are provided in the ESI.† The crystal structures of each chiral HMH incorporated with different achiral ligands are determined by single crystal X-ray diffraction (SCXRD). The phase purity of all compounds is examined by powder X-ray diffraction (PXRD) characterization (Fig. S1†). The actual concentration of the Sb^{3+} dopant is determined by inductively coupled plasma mass spectrometry (ICP-MS), and the results reveal that the actual molar ratio of Sb/In of all compounds is 0.05/0.95 (Table S1†). For convenience, the R-configuration is selected as the representative of each pair of compounds, as the structures of R- and S- enantiomers are identical. As shown in Fig. 1a and b, R-1 and R-2 show typical 0D structural features, where anionic $[In/SbCl_6]^{3-}$ octahedra are fully separated by organic ligands.[17,18,36,37] Both R-1 and R-2 crystallize in the Sohncke space group of $C2$ (Table S2†). The R-MBA and achiral ligands in both R-1 and R-2 are arranged around each $[In/SbCl_6]^{3-}$ octahedron in a 4 : 2 manner, with the planes of the benzene ring of R-MBA being parallel to the c-axis, and the planes of C–N–C (2MA) and C–C–C (3MA) being perpendicular to the c-axis. The arrangement and molar ratio of organic ligands around inorganic octahedra can also be clearly seen from the a-axis (Fig. S2†).

Despite the congruence in the space group, crystal structure, and the molar ratios of chiral and achiral ligands between compounds R-1 and R-2, a significant disparity emerges in the distribution and strength of hydrogen bonds between organic ligands and inorganic octahedra. These deviations originate from the use of different achiral ligands in R-1 and R-2. As shown in Fig. 1c and d, the H···Cl distances between organic ligands and inorganic octahedra are measured to be 2.47–2.78 Å for R-1 and 2.14–2.41 Å for R-2, respectively, indicating the stronger hydrogen bonds in R-2. Moreover, the N–H···Cl angles are closer to 180° in R-2, further indicating stronger hydrogen bonds (Fig. S3†).[38] To clearly visualize the hydrogen bond distribution around the inorganic octahedron, the hydrogen bonds along three different axes are represented by colored arrows. As shown in Fig. 1e, all the strong and weak hydrogen bonds between organic ligands and inorganic octahedra in R-1 are aligned in the equatorial Cl–In/Sb–Cl plane, designated as type I. Consequently, the In/Sb–Cl bonds in these two axes are simultaneously elongated, with the bond lengths of 2.57 and 2.54 Å, respectively. The In/Sb–Cl bonds in the vertical axis without hydrogen bonding interactions have relatively shorter lengths of 2.47 Å. In contrast, the hydrogen bonds in R-2 are present in a distinct distribution, denoted as type II (Fig. 1f). The presence of only one strong hydrogen bond in the two axes in the equatorial Cl–In/Sb–Cl plane (indicated by red arrows) results in the elongation of these two In/Sb–Cl bonds, with the bond lengths of 2.53 and 2.49 Å, respectively. Conversely, the weak hydrogen bonds (denoted by blue arrows) in the vertical axis yield the In/Sb–Cl bond lengths of 2.55 Å. Overall, the distinct distribution and strength of hydrogen bonds lead to varied octahedral distortions. Based on the refined crystal structures, the distortions of inorganic octahedra are quantitatively assessed by adopting an off-centering distortion index ($\mathcal{D}$) to evaluate their dissymmetry (eqn (1)):[39]

$$\mathcal{D} = \sum_{i=1}^{3} \frac{|a_i - b_i|}{a_i + b_i} \quad (1)$$

where a_i and b_i refer to the short and long In/Sb–Cl bond lengths along one axis, respectively. The $\mathcal{D}$ values of R-1 and R-2 are estimated to be 0.012 and 0.020, respectively, which are

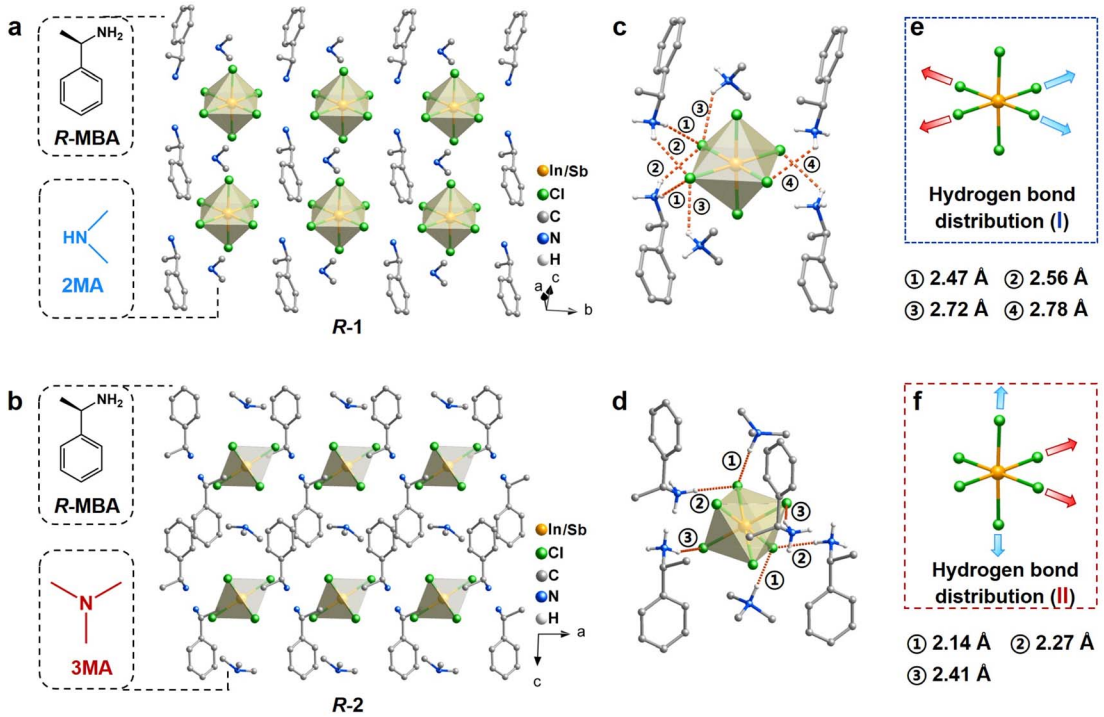

Fig. 1 (a and b) Schematic crystal structures of *R*-1 and *R*-2, respectively. Hydrogen atoms are omitted for clarity. (c and d) Schematic structures of the hydrogen bonds between inorganic $[In/SbCl_6]^{3-}$ octahedra and organic ligands in *R*-1 and *R*-2, respectively. The hydrogen bonds between organic ligands and inorganic octahedra are highlighted in dotted lines. (e and f) Hydrogen bond distribution in *R*-1 and *R*-2, respectively.

primarily determined by the distribution type of hydrogen bonds formed with the octahedra. The larger $\mathcal{D}$ value of the octahedron can be attained when the distribution of hydrogen bonds is asymmetrical, like type II.

To examine the effect of the $\mathcal{D}$ parameter on chiroptical properties, a series of photophysical characterization studies were conducted. As shown in Fig. 2a, *R*-1 and *R*-2 exhibit obvious absorptions in the 270–405 nm range, which are different from the absorption spectra of $(R\text{-MBA})_2(2MA)InCl_6$ and $(R\text{-MBA})_2(3MA)InCl_6$ in the 270–290 nm range (Fig. S4†). These differences indicate that these absorptions in *R*-1 and *R*-2 originate from the optically active antimony halogen octahedra. Under 325 nm excitation, the PL emission spectra of *R*-1 and *R*-2 exhibit broad emissions peaked at 600 and 590 nm, respectively (Fig. 2b). The PL excitation (PLE) spectra are located in the range of 270–405 nm, consistent with their corresponding absorption spectra (Fig. S5a†). The remarkable near-unity PLQYs are recorded for *R*-1 and *R*-2. To reveal the origins of the broadband emission, excitation-dependent, time-resolved and power-dependent PL spectra are measured. The PL spectra obtained at various excitation wavelengths exhibit identical profiles, confirming that the broad emissions originate from the same excited states (Fig. S5b and c†). The PL lifetimes of *R*-1 and *R*-2 are measured to be 3.80 and 3.27 μs, respectively (Fig. S6†). The microsecond PL lifetimes indicate that the emission arises from inorganic modules, rather than from the organic ligands with nanosecond PL lifetimes (Fig. S7†). The linear excitation power-dependent PL intensities rule out the possibility of defect-related emissions (Fig. S8†).[40–42] Moreover, these PL spectra and PL lifetimes are obviously different from their pristine counterparts, which exhibit excitation-dependent PL spectra and longer PL lifetimes (Fig. S9 and 10†). Therefore, these broad emissions with high PLQYs are assigned to the Sb^{3+}-related emissions. Such high PLQYs benefit from their intrinsic 0D structure with isolated inorganic octahedra, which exhibit strong quantum confinement effects.[36,43] These broadband and large Stokes-shifted PL characteristics of *R*-1 and *R*-2 are well consistent with those of recently reported Sb-based HMHs.[44–49]

To shed light on the role of structural variations in inorganic octahedra in determining chiroptical activities, solid-state circular dichroism (CD) and CPL spectra of chiral HMHs are measured and compared. As shown in Fig. 2c, the CD spectra of chiral *R*/*S*-1 and *R*/*S*-2 exhibit obvious Cotton effects in the range of 270–405 nm, which agree well with their corresponding absorption spectra but differ from those of *R*/*S*-MBA, implying that the observed CD signals originate from inorganic octahedra.[25] All *R*-configurations of chiral HMHs exhibit negative peaks in the range of 270–405 nm regardless of the type of achiral ligands. As the same amounts of samples are used for CD characterization, *R*-1 exhibits a small |CD| value (6.57 mdeg), while *R*-2 reveals a significantly enhanced |CD| signal (23.3 mdeg). To quantitatively assess this difference, the absorption dissymmetry factor g_{abs} is calculated using eqn (2):[50]

$$g_{abs} = \frac{CD}{32\,980 \times absorbance} \quad (2)$$

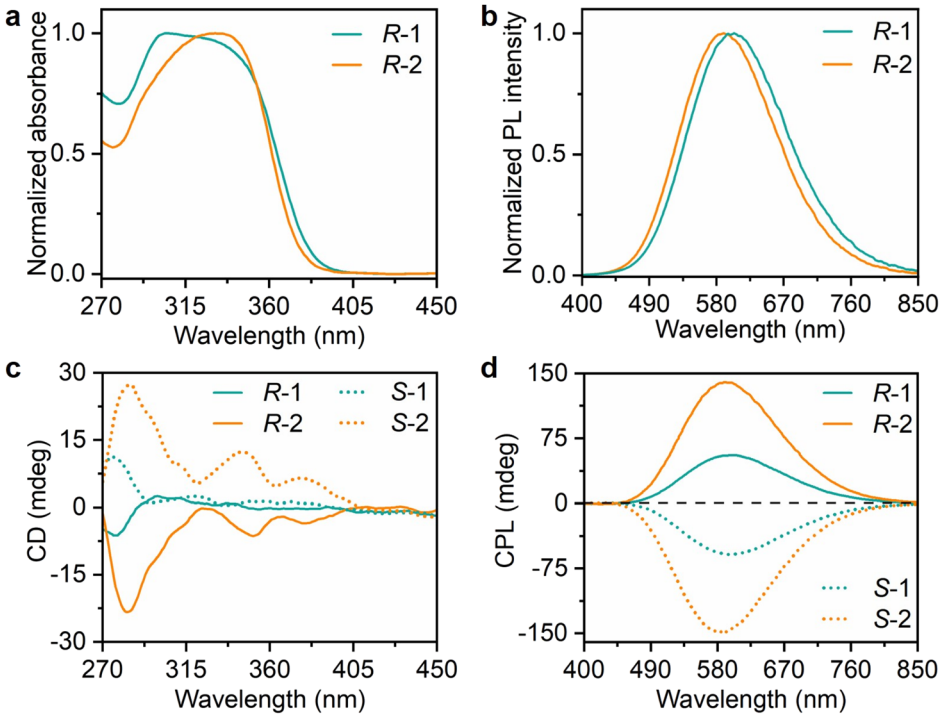

Fig. 2 Optical properties of *R*-1 and *R*-2. (a) Normalized UV-Vis absorption spectra, (b) normalized PL emission spectra, (c) CD spectra and (d) CPL spectra of *R*-1 and *R*-2.

where the CD (in mdeg) and the absorbance can be obtained from CD spectral measurement. The calculated g_{abs} value is thus independent of pellet thickness, sample concentration and molecular weight. As shown in Fig. S11,† the local value of g_{abs} is significantly enhanced from 1.6×10^{-4} (400 nm, *R*-1) to 3.9×10^{-4} (400 nm, *R*-2), corresponding to a 2.4-fold improvement. As CD spectra are associated with ground state properties, it is reasonable to infer that the chiroptical activities of chiral HMHs in the ground state can be enhanced by increasing the $\mathcal{D}$ parameter of inorganic octahedra. At the same time, CPL spectra reflect the excited state properties of chiral systems. As shown in Fig. 2d, both *R*/*S*-1 and *R*/*S*-2 enantiomers show mirror symmetrical curves in their CPL spectra, which match well with their corresponding PL spectra, suggesting that the CPL signals originate from the inorganic octahedra. The CPL magnitude is quantitively evaluated by the luminescence dissymmetry factor $g_{lum} = 2(I_L - I_R)/(I_L + I_R)$, where I_L and I_R represent the intensities of left- and right-handed CPL, respectively.[51] The g_{lum} values calculated from these CPL spectra are 7.8×10^{-3} for *R*-1 and 2.0×10^{-2} for *R*-2, corresponding to a 2.6-fold enhancement from *R*-1 to *R*-2 (Fig. S12†). Such CPL analyses reveal that the excited state chirality of these HMHs can be also improved with increasing the $\mathcal{D}$ parameter.

As previously demonstrated, chiroptical activities in HMHs originate from inorganic modules due to the chirality induction *via* N–H···Cl hydrogen bonds.[22,31–33] To clearly reveal the relationship between the chiroptical performance and the distortion of inorganic octahedra, detailed structural analyses of inorganic octahedra in *R*-1 and *R*-2 are conducted. To quantify the distortion of $[In/SbCl_6]^{3-}$ octahedra in *R*-1 and *R*-2, both bond length distortion and bond angle distortion are calculated.[52,53] As shown in Table S3,† the bond length distortions of *R*-1 and *R*-2 are calculated to be 2.76×10^{-4} and 1.1×10^{-4}, respectively, and the bond angle distortions of *R*-1 and *R*-2 are 3.73 and 1.27, respectively. It is clear that the extent of bond length and bond angle distortion in these 0D HMHs varies inversely with the values of $|g_{abs}|$ and $|g_{lum}|$, although the bond angle distortion of the inorganic framework in 2D HMHs could promote their chiroptical properties.[32] As demonstrated above, the values of $|g_{abs}|$ and $|g_{lum}|$ increase with larger values of the $\mathcal{D}$ parameter, suggesting that the augmentation in chiroptical activity is correlated with the increased off-centering distortion of inorganic octahedra. To support this claim, a series of control experiments are carried out to elucidate the relationship between the $\mathcal{D}$ parameter and the magnitudes of $|g_{abs}|$ and $|g_{lum}|$.

With continuously increasing the Sb^{3+} concentration, three pairs of enantiomorphic $(R/S\text{-MBA})_2(3MA)In_{0.79}Sb_{0.21}Cl_6$ (*R*/*S*-2A), $(R/S\text{-MBA})_2(3MA)In_{0.72}Sb_{0.28}Cl_6$ (*R*/*S*-2B) and $(R/S\text{-MBA})_2(3MA)In_{0.59}Sb_{0.41}Cl_6$ (*R*/*S*-2C) are accordingly synthesized. Structural and composition characterization studies demonstrate their crystal structure, phase purity and actual Sb^{3+} dopant concentration (Fig. S13, 14, Tables S4 and 5†). The lattice constants (*b* and *c* axes) and angles (α, β, γ) remain nearly constant with increasing Sb^{3+} dopant concentration due to the similar ionic radii of In^{3+} (80 pm) and Sb^{3+} (76 pm) (Fig. S15†). The *a*-axis length slightly increases due to the synergetic effect of the similar ionic radii of In^{3+} and Sb^{3+} and decreased ionic bond polarity after the substitution of Sb^{3+}.[54] Similar to *R*-2, *R*-2A, *R*-2B and *R*-2C show typical 0D structures with inorganic

octahedra fully isolated by organic ligands. The distribution of hydrogen bonds (type II) in these compounds is independent of Sb^{3+} dopant concentration (Fig. S13†), however, the strength of hydrogen bonds changes with Sb^{3+} dopant content. Specifically, the strength of hydrogen bonds demonstrates a positive correlation with the concentration of Sb^{3+} (Fig. S13†), as demonstrated by the shorter distance between N atoms and Cl^- ions and increased N–H···Cl angles (Fig. S16 and Table S6†). Thus, the In/Sb–Cl bonds involved in the formation of hydrogen bonds are further elongated from 2.56 to 2.62 Å, as the Sb^{3+} dopant concentration increases (Fig. 3a). Simultaneously, the $\mathcal{D}$ parameter changes and follows the trend of *R*-2A (2.4×10^{-2}) < *R*-2B (3.1×10^{-2}) < *R*-2C (4.7×10^{-2}), indicating that the $\mathcal{D}$ parameter increases with increasing the Sb^{3+} dopant concentration.

R-2A, *R*-2B and *R*-2C all show identical yellow emissions with high PLQYs of near-unity (Fig. S17a†). Moreover, their microsecond PL lifetimes, excitation-independent PL spectra and linearly fitted power-dependent data demonstrate that these bright emissions originate from Sb^{3+}, similar to *R*-2 (Fig. S17 and 18†). The CD spectra of these three chiral HMHs exhibit obvious Cotton effects in the range of 270–450 nm (Fig. S19†). The magnitude of $|g_{abs}|$ increases from 0.78×10^{-3} (at 400 nm, *R*-2A) to 1.25×10^{-3} (at 400 nm, *R*-2C) corresponding to a 1.6-fold enhancement, and follows the trend of *R*-2A < *R*-2B < *R*-2C (Fig. 3b). Intriguingly, the CPL intensities of chiral HMHs are enhanced with increasing Sb^{3+} concentration (Fig. S20†). The $|g_{lum}|$ values also show the trend of *R*-2A (2.2×10^{-2}) < *R*-2B (3.0×10^{-2}) < *R*-2C (3.8×10^{-2}), which is in line with $|g_{abs}|$ (Fig. 3c). By plotting the $|g_{abs}|$ and g_{lum} values and corresponding $\mathcal{D}$ parameters of all chiral HMHs, it is found that the $|g_{abs}|$ and g_{lum} values are positively proportional to the $\mathcal{D}$ parameter (Fig. 3d and e). Moreover, the bond length and bond angle distortion exhibit totally different variations compared to $\mathcal{D}$ parameters (Fig. S21†). These results clearly demonstrate that a large $\mathcal{D}$ parameter of inorganic octahedra in chiral HMHs is crucial to enhancing the values of $|g_{abs}|$ and $|g_{lum}|$. Furthermore, the g_{lum} value ($+3.8 \times 10^{-2}$) and PLQY (near-unity) of *R*-2C exceed the CPL performances of currently reported chiral HMHs (Table S8†).

Based on the above crystallographic and chiroptical spectra studies, a plausible mechanism to enhance the values of $|g_{abs}|$ and $|g_{lum}|$ in 0D HMHs is proposed (Fig. 4):

(i) The coexistence of chiral *R*-MBA and achiral 2MA ligands induces the formation of asymmetric hydrogen bonds between organic ligands and inorganic octahedra $[In/SbCl]_6^{3-}$. As strong and weak hydrogen bonds are aligned along the same axis of equatorial Cl–In/Sb–Cl with opposite directions (type I), inorganic octahedra with small off-centering distortion can be observed;

(ii) Substituting 2MA with the 3MA ligand that is a stronger hydrogen bond acceptor and has a greater steric hindrance results in the distribution of strong and weak hydrogen bonds surrounding inorganic octahedra along two distinct axes of equatorial Cl–In/Sb–Cl (type II). Compared with type I, the off-centering distortion of inorganic octahedra in type II is obviously enhanced. Accordingly, the $|g_{abs}|$ and $|g_{lum}|$ values of chiral 0D HMHs in type II surpass those of type I, despite having identical crystal structures, inorganic components, and PLQYs;

(iii) The off-centering distortion of inorganic octahedra in type II can be further enhanced by increasing the Sb^{3+} dopant concentration. The higher electronegativity of Sb^{3+} compared to

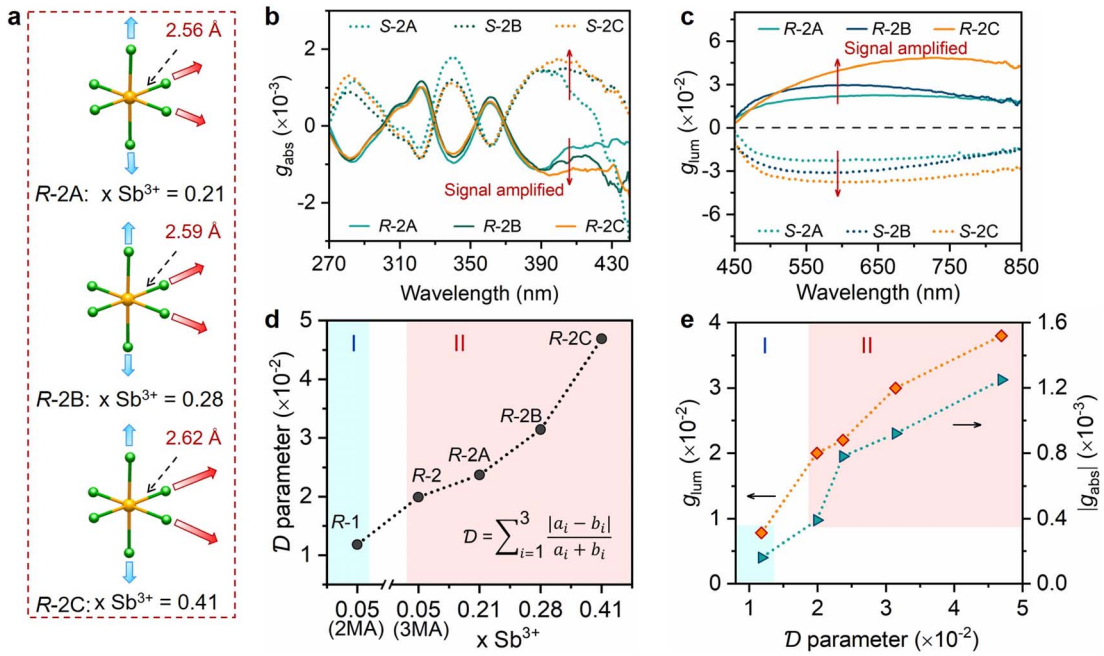

Fig. 3 (a) Schematic of the $[In_{1-x}Sb_xCl]_6^{3-}$ octahedra with continuously increasing the Sb^{3+} dopant concentration. g_{abs} (b) and g_{lum} (c) spectra of *R*/*S*-2A, *R*/*S*-2B and *R*/*S*-2C. (d) Plots of $\mathcal{D}$ parameter *versus* Sb^{3+} dopant concentration. (e) Plots of calculated $|g_{abs}|$ values at 400 nm and local maximum $|g_{lum}|$ values as a function of the $\mathcal{D}$ parameter.

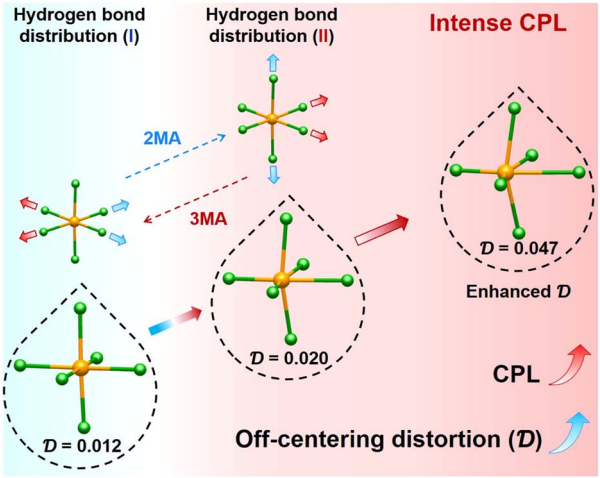

Fig. 4 Schematic illustration of the stepwise chirality enhancement mechanism of chiral HMHs.

In^{3+} results in reduced distances between N atoms and Cl^- ions, thereby reinforcing the strong hydrogen bonds and amplifying the asymmetric stretch of In/Sb–Cl bonds. Consequently, both $|g_{abs}|$ and $|g_{lum}|$ values increase with the increase of off-centering distortion of inorganic octahedra.

Such outstanding CPL performances make *R*/*S*-2C promising candidates for CPL light sources. *R*/*S*-2C are therefore used as the phosphors to emit CPL. *R*/*S*-light-emitting diodes (*R*/*S*-LEDs) are fabricated by coating *R*/*S*-2C polycrystals onto 365 nm ultraviolet GaN LED chips. The ultraviolet emission of the GaN chip is turned on at 3.0 V, which excites the *R*/*S*-2C polycrystals to generate CPL. CPL characterization studies of *R*/*S*-LEDs are performed on a JASCO CPL-300 through inserting the fabricated LED into the sample chamber and blocking the xenon lamp light source. These *R*/*S*-LEDs exhibit bright yellow emissions, and their CPL spectra show a mirror image profile (Fig. 5a). The polarized degree (*P*) is used to evaluate the CPL performance of *R*/*S*-LEDs, which is defined as

$$P = \frac{I_L - I_R}{I_L + I_R} \times 100\%$$

where I_L and I_R are the intensities of left and right CPL, respectively. It can be inferred that $P = (g_{lum}/2) \times 100\%$. The g_{lum} values of *R*/*S*-LEDs are $\pm 3.2 \times 10^{-2}$, so the *P* values of *R*/*S*-LEDs are calculated to be ±1.6% at 590 nm (Fig. 5b). To test the color stability of the fabricated *R*/*S*-LEDs, electro-luminescence (EL) spectra are collected at varied driving currents. As shown in Fig. 5c, the EL spectra of the *R*-LED exhibit identical shapes at different driving currents (5–100 mA). Besides, the chromaticity coordinate (0.50, 0.46) of the *R*-LED remains nearly unchanged,

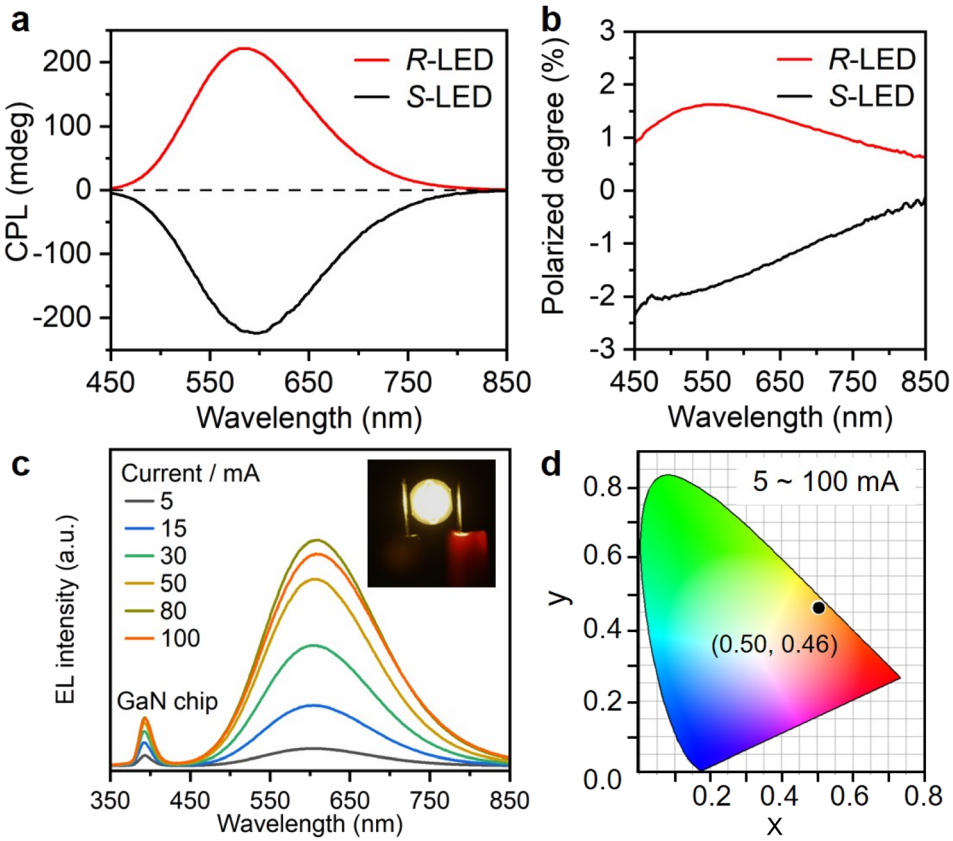

Fig. 5 (a) CPL spectra of *R*/*S*-LEDs fabricated by encapsulating *R*/*S*-2C polycrystals onto a 365 nm ultraviolet GaN LED chip. (b) Polarized degree of the *R*/*S*-LED devices. The CPL characterization of the LED devices powered by 3.0 V. (c) EL spectra and (d) chromaticity coordinates of the *R*-LED at different driving currents (5–100 mA). Inset of (c): photographs of the fabricated LEDs under operation.

suggesting the excellent color stability of the *R*-LED (Fig. 5d). These results clearly demonstrate the feasibility of utilizing *R*/*S*-2C for CPL light sources.

Conclusions

In summary, five pairs of enantiomorphic *R*/*S*-1, *R*/*S*-2, *R*/*S*-2A, *R*/*S*-2B and *R*/*S*-2C chiral 0D indium-antimony HMHs based on achiral ligands 2MA and 3MA and different Sb^{3+} dopant concentrations are prepared. Among these, *R*-2C exhibits the largest $|g_{lum}|$ value of 3.8×10^{-2}, as well as high PLQY of near-unity, outperforming currently reported chiral HMHs. Structural analyses and photophysical characterization studies reveal that the large off-centering distortion of inorganic octahedra, which is determined by the distribution and strength of hydrogen bonds formed around inorganic octahedra, plays critical roles in achieving higher g_{abs} and g_{lum} values. Furthermore, *R*/*S*-LEDs with ±1.6% polarized degree are prepared, providing a feasible strategy to fabricate an efficient UV-pumped CPL light source. This work not only provides a general strategy to improve g_{abs}/g_{lum} values of chiral 0D HMHs, but also sheds light on the relationship between the structure of the inorganic unit and chiroptical activity.

Data availability

Additional data supporting the findings described in this paper are available in the ESI.† Crystallographic data for the structures reported in the present article have been deposited at the Cambridge Crystallographic Data Center (CCDC). The accession CCDC numbers for *R*-1, *R*-2, *R*-2A, *R*-2B and *R*-2C crystal structure CIFs reported in this paper are: 2344292, 2344293, 2344294, 2344295 and 2344296. These data are provided free of charge by the joint CCDC and Fachinformationszentrum Karlsruhe Access Structures service.

Author contributions

Z. Q. and Y. L. proposed and supervised the project; Y. L. designed the experiments, analyzed the data and wrote the paper; Y. W., Z. L., and B. X. participated in discussions and gave much helpful advice; M. H. helped with the PXRD measurements; P. H. helped with power-dependent PL measurements; C. L. helped with the PL measurements of chiral ligands.

Conflicts of interest

There are no conflicts to declare.

Acknowledgements

This work was supported by the National Natural Science Foundation of China (NSFC) (22375084), the Guangdong Education Department (2021ZDZX2049), and the Shenzhen Science and Technology Innovation Committee (RCJC20210609104444106 8, RCBS20221008093335082, and KCXFZ20211020174805008). The computational resource was supported by the Center for Computational Science and Engineering at the Southern University of Science and Technology (SUSTech).

References

1 X. Q. Zhan, F. F. Xu, Z. H. Zhou, Y. L. Yan, J. N. A. Yao and Y. S. Zhao, 3D Laser Displays Based on Circularly Polarized Lasing from Cholesteric Liquid Crystal Arrays, *Adv. Mater.*, 2021, **33**, 2104418.

2 J. F. Sherson, H. Krauter, R. K. Olsson, B. Julsgaard, K. Hammerer, I. Cirac and E. S. Polzik, Quantum Teleportation Between Light and Matter, *Nature*, 2006, **443**, 557–560.

3 Y. Kan, S. K. H. Andersen, F. Ding, S. Kumar, C. Zhao and S. I. Bozhevolnyi, Metasurface-Enabled Generation of Circularly Polarized Single Photons, *Adv. Mater.*, 2020, **32**, 1907832.

4 J. Zhang, M. Calame and M. L. Perrin, Contacting Atomically Precise Graphene Nanoribbons for Next-Generation Quantum Electronics, *Matter*, 2022, **5**, 2497–2499.

5 M. Zhang, Q. Guo, Z. Li, Y. Zhou, S. Zhao, Z. Tong, Y. Wang, G. Li, S. Jin, M. Zhu, T. Zhuang and S.-H. Yu, Processable Circularly Polarized Luminescence Material Enables Flexible Stereoscopic 3D Imaging, *Sci. Adv.*, 2023, **9**, eadi9944.

6 H. Z. Zheng, W. R. Li, W. Li, X. J. Wang, Z. Y. Tang, S. X. A. Zhang and Y. Xu, Uncovering the Circular Polarization Potential of Chiral Photonic Cellulose Films for Photonic Applications, *Adv. Mater.*, 2018, **30**, 1705948.

7 J. Ahn, E. Lee, J. Tan, W. Yang, B. Kim and J. Moon, A New Class of Chiral Semiconductors: Chiral-Organic-Molecule-Incorporating Organic-Inorganic Hybrid Perovskites, *Mater. Horiz.*, 2017, **4**, 851–856.

8 J. Q. Ma, C. Fang, C. Chen, L. Jin, J. Q. Wang, S. Wang, J. Tang and D. H. Li, Chiral 2D Perovskites with a High Degree of Circularly Polarized Photoluminescence, *ACS Nano*, 2019, **13**, 3659–3665.

9 J. X. Gao, W. Y. Zhang, Z. G. Wu, Y. X. Zheng and D. W. Fu, Enantiomorphic Perovskite Ferroelectrics with Circularly Polarized Luminescence, *J. Am. Chem. Soc.*, 2020, **142**, 4756–4761.

10 H. Duim and M. A. Loi, Chiral Hybrid Organic-Inorganic Metal Halides: A Route Toward Direct Detection and Emission of Polarized Light, *Matter*, 2021, **4**, 3835–3851.

11 A. Pietropaolo, A. Mattoni, G. Pica, M. Fortino, G. Schifino and G. Grancini, Rationalizing the Design and Implementation of Chiral Hybrid Perovskites, *Chem*, 2022, **8**, 1231–1253.

12 X. Han, P. Cheng, S. Han, Z. Wang, J. Guan, W. Han, R. Shi, S. Chen, Y. Zheng, J. Xu and X. H. Bu, Multi-stimuli-responsive Luminescence Enabled by Crown Ether Anchored Chiral Antimony Halide Phosphors, *Chem. Sci.*, 2024, **15**, 3530–3538.

13 X. Y. Niu, Z. C. Zeng, Z. Y. Wang, H. L. Lu, B. Sun, H. L. Zhang, Y. S. Chen, Y. P. Du and G. K. Long, The First

Chiral Cerium Halide Towards Circularly-Polarized Luminescence in The UV Region, *Sci. China: Chem.*, 2024, **67**, 1961–1968.

14 D. Y. Liu, H. Y. Li, R. P. Han, H. L. Liu and S. Q. Zang, Multiple Stimuli-Responsive Luminescent Chiral Hybrid Antimony Chlorides for Anti-Counterfeiting and Encryption Applications, *Angew. Chem., Int. Ed.*, 2023, **62**, e202307875.

15 Q. W. Guan, H. Ye, T. T. Zhu, X. Y. Zhang, S. H. You, J. B. Wu, Y. X. Zheng, X. T. Liu and J. H. Luo, Formamidine Engineering the Lattice Distortion of Chiral Halide Perovskites for Efficient Blue Circularly Polarized Emission, *Adv. Opt. Mater.*, 2023, **11**, 2202726.

16 Z.-L. Gong, X. Zhu, Z. Zhou, S.-W. Zhang, D. Yang, B. Zhao, Y.-P. Zhang, J. Deng, Y. Cheng, Y.-X. Zheng, S.-Q. Zang, H. Kuang, P. Duan, M. Yuan, C.-F. Chen, Y. S. Zhao, Y.-W. Zhong, B. Z. Tang and M. Liu, Frontiers in Circularly Polarized Luminescence: Molecular Design, Self-Assembly, Nanomaterials, and Applications, *Sci. China: Chem.*, 2021, **64**, 2060–2104.

17 M. Z. Li and Z. G. Xia, Recent Progress of Zero-Dimensional Luminescent Metal Halides, *Chem. Soc. Rev.*, 2021, **50**, 2626–2662.

18 K. M. McCall, V. Morad, B. M. Benin and M. V. Kovalenko, Efficient Lone-Pair-Driven Luminescence: Structure–Property Relationships in Emissive $5s^2$ Metal Halides, *ACS Mater. Lett.*, 2020, **2**, 1218–1232.

19 T. Cai, W. W. Shi, R. Z. Wu, C. Chu, N. Jin, J. Y. Wang, W. W. Zheng, X. Z. Wang and O. Chen, Lanthanide Doping into All-Inorganic Heterometallic Halide Layered Double Perovskite Nanocrystals for Multimodal Visible and Near-Infrared Emission, *J. Am. Chem. Soc.*, 2024, **146**, 3200–3209.

20 G. K. Long, R. Sabatini, M. I. Saidaminov, G. Lakhwani, A. Rasmita, X. G. Liu, E. H. Sargent and W. B. Gao, Chiral-Perovskite Optoelectronics, *Nat. Rev. Mater.*, 2020, **5**, 423–439.

21 H. L. Xuan, J. L. Li, L. J. Xu, D. S. Zheng and Z. N. Chen, Circularly Polarized Luminescence based on 0D Lead-Free Antimony (III) Halide Hybrids, *Adv. Opt. Mater.*, 2022, **10**, 2200591.

22 Y. Wei, C. Li, Y. W. Li, Z. S. Luo, X. Y. Wu, Y. L. Liu, L. M. Zhang, X. He, W. Wang and Z. W. Quan, Circularly Polarized Luminescence from Zero-Dimensional Hybrid Lead-Tin Bromide with Near-Unity Photoluminescence Quantum Yield, *Angew. Chem., Int. Ed.*, 2022, **61**, e202212685.

23 M. P. Davydova, L. Q. Meng, M. I. Rakhmanova, I. Y. Bagryanskaya, V. S. Sulyaeva, H. Meng and A. V. Artem'ev, Highly Emissive Chiral Mn(II) Bromide Hybrids for UV-Pumped Circularly Polarized LEDs and Scintillator Image Applications, *Adv. Opt. Mater.*, 2023, **11**, 2202811.

24 J. J. Guan, Y. S. Zheng, P. X. Cheng, W. Q. Han, X. Han, P. H. Wang, M. Y. Xin, R. C. Shi, J. L. Xu and X. H. Bu, Free Halogen Substitution of Chiral Hybrid Metal Halides for Activating the Linear and Nonlinear Chiroptical Properties, *J. Am. Chem. Soc.*, 2023, **145**, 26833–26842.

25 Y. L. Liu, Z. S. Luo, Y. Wei, C. Li, Y. L. Chen, X. He, X. Y. Chang and Z. W. Quan, Integrating Achiral and Chiral Organic Ligands in Zero-Dimensional Hybrid Metal Halides to Boost Circularly Polarized Luminescence, *Angew. Chem., Int. Ed.*, 2023, **62**, e202306821.

26 Y. Deng, F. Li, Z. Zhou, M. Wang, Y. Zhu, J. Zhao, S. Liu and Q. Zhao, Chiral Induction and Sb^{3+} Doping in Indium Halides to Trigger Second Harmonic Generation and Circularly Polarized Luminescence, *Chin. Chem. Lett.*, 2024, **35**, 109085.

27 G. K. Long, C. Y. Jiang, R. Sabatini, Z. Y. Yang, M. Y. Wei, L. N. Quan, Q. M. Liang, A. Rasmita, M. Askerka, G. Walters, X. W. Gong, J. Xing, X. L. Wen, R. Quintero-Bermudez, H. F. Yuan, G. C. Xing, X. R. Wang, D. T. Song, O. Voznyy, M. T. Zhang, S. Hoogland, W. B. Gao, Q. H. Xiong and E. H. Sargent, Spin Control in Reduced-Dimensional Chiral Perovskites, *Nat. Photonics*, 2018, **12**, 528–533.

28 T. T. Zhu, W. Weng, C. M. Ji, X. Y. Zhang, H. Ye, Y. P. Yao, X. L. Li, J. L. Li, W. X. Lin and J. H. Luo, Chain-to-Layer Dimensionality Engineering of Chiral Hybrid Perovskites to Realize Passive Highly Circular-Polarization-Sensitive Photodetection, *J. Am. Chem. Soc.*, 2022, **144**, 18062–18068.

29 Y. S. Zheng, X. Han, P. X. Cheng, X. D. Jia, J. L. Xu and X. H. Bu, Induction of Chiral Hybrid Metal Halides from Achiral Building Blocks, *J. Am. Chem. Soc.*, 2022, **144**, 16471–16479.

30 W. D. Cai, J. J. Qin, T. Q. Pang, X. Y. Cai, R. X. Jia and F. Gao, Chirality Induced Crystal Structural Difference in Metal Halide Composites, *Adv. Opt. Mater.*, 2022, **10**, 2102140.

31 S. Ma, Y. K. Jung, J. Ahn, J. Kyhm, J. Tan, H. Lee, G. Jang, C. U. Lee, A. Walsh and J. Moon, Elucidating the Origin Of Chiroptical Activity in Chiral 2D Perovskites through Nano-Confined Growth, *Nat. Commun.*, 2022, **13**, 3259.

32 J. Son, S. Ma, Y. K. Jung, J. Tan, G. Jang, H. Lee, C. U. Lee, J. Lee, S. Moon, W. Jeong, A. Walsh and J. Moon, Unraveling Chirality Transfer Mechanism by Structural Isomer-Derived Hydrogen Bonding Interaction in 2D Chiral Perovskite, *Nat. Commun.*, 2023, **14**, 3124.

33 M. K. Jana, R. Y. Song, H. L. Liu, D. R. Khanal, S. M. Janke, R. D. Zhao, C. Liu, Z. V. Vardeny, V. Blum and D. B. Mitzi, Organic-To-Inorganic Structural Chirality Transfer in a 2D Hybrid Perovskite and Impact on Rashba-Dresselhaus Spin-Orbit Coupling, *Nat. Commun.*, 2020, **11**, 4699.

34 K. J. Liu, J. Zhao and Q. L. Liu, Chiral Organic Cations and Distorted Inorganic Polyhedra Composing Metal Halide Nonlinear Optical Materials, *Laser Photonics Rev.*, 2024, 2400345.

35 H. P. Lu, Z. V. Vardeny and M. C. Beard, Control of Light, Spin and Charge with Chiral Metal Halide Semiconductors, *Nat. Rev. Chem*, 2022, **6**, 470–485.

36 H. R. Lin, C. K. Zhou, Y. Tian, T. Siegrist and B. W. Ma, Low-Dimensional Organometal Halide Perovskites, *ACS Energy Lett.*, 2018, **3**, 54–62.

37 S. Q. Sun, M. Lu, X. P. Gao, Z. F. Shi, X. Bai, W. W. Yu and Y. Zhang, 0D Perovskites: Unique Properties, Synthesis, and Their Applications, *Adv. Sci.*, 2021, **8**, e2102689.

38 E. Arunan, G. R. Desiraju, R. A. Klein, J. Sadlej, S. Scheiner, I. Alkorta, D. C. Clary, R. H. Crabtree, J. J. Dannenberg, P. Hobza, H. G. Kjaergaard, A. C. Legon, B. Mennucci and D. J. Nesbitt, Definition of the hydrogen bond (IUPAC Recommendations 2011), *Pure Appl. Chem.*, 2011, **83**, 1637–1641.

39 X. J. Lü, C. Stoumpos, Q. Y. Hu, X. D. Ma, D. Z. Zhang, S. H. Guo, J. Hoffman, K. J. Bu, X. F. Guo, Y. Q. Wang, C. Ji, H. J. Chen, H. W. Xu, Q. X. Jia, W. G. Yang, M. G. Kanatzidis and H. K. Mao, Regulating Off-Centering Distortion Maximizes Photoluminescence in Halide Perovskites, *Natl. Sci. Rev.*, 2021, **8**, nwaa288.

40 G. H. Wu, C. K. Zhou, W. M. Ming, D. Han, S. Y. Chen, D. Yang, T. Besara, J. Neu, T. Siegrist, M. H. Du, B. W. Ma and A. G. Dong, A One-Dimensional Organic Lead Chloride Hybrid with Excitation-Dependent Broadband Emissions, *ACS Energy Lett.*, 2018, **3**, 1443–1449.

41 T. Schmidt, G. Daniel and K. Lischka, The Excitation Power Dependence of the near Band Edge Photoluminescence of II-VI Semiconductors, *J. Cryst. Growth*, 1992, **117**, 748–752.

42 T. Schmidt, K. Lischka and W. Zulehner, Excitation-Power Dependence of The Near-Band-Edge Photoluminescence of Semiconductors, *Phys. Rev. B*, 1992, **45**, 8989–8994.

43 S. R. Li, J. J. Luo, J. Liu and J. Tang, Self-Trapped Excitons in All-Inorganic Halide Perovskites: Fundamentals, Status, and Potential Applications, *J. Phys. Chem. Lett.*, 2019, **10**, 1999–2007.

44 Z. P. Wang, Z. Z. Zhang, L. Q. Tao, N. N. Shen, B. Hu, L. K. Gong, J. R. Li, X. P. Chen and X. Y. Huang, Hybrid Chloroantimonates(III): Thermally Induced Triple-Mode Reversible Luminescent Switching and Laser- Printable Rewritable Luminescent Paper, *Angew. Chem., Int. Ed.*, 2019, **58**, 9974–9978.

45 G. M. Song, M. Z. Li, S. Z. Zhang, N. Z. Wang, P. F. Gong, Z. G. Xia and Z. S. Lin, Enhancing Photoluminescence Quantum Yield in 0D Metal Halides by Introducing Water Molecules, *Adv. Funct. Mater.*, 2020, **30**, 2002468.

46 L. J. Xu, A. Plaviak, X. Lin, M. Worku, Q. He, M. Chaaban, B. J. Kim and B. Ma, Metal Halide Regulated Photophysical Tuning of Zero-Dimensional Organic Metal Halide Hybrids: From Efficient Phosphorescence to Ultralong Afterglow, *Angew. Chem., Int. Ed.*, 2020, **59**, 23067–23071.

47 F. Liu, T. J. Zhang, D. Mondal, S. Y. Teng, Y. Zhang, K. K. Huang, D. Y. Wang, W. S. Yang, P. Mahadevan, Y. S. Zhao, R. G. Xie and N. Pradhan, Light-Emitting Metal-Organic Halide 1D and 2D Structures: Near-Unity Quantum Efficiency, Low-Loss Optical Waveguide and Highly Polarized Emission, *Angew. Chem., Int. Ed.*, 2021, **60**, 13548–13553.

48 V. Morad, S. Yakunin, B. M. Benin, Y. Shynkarenko, M. J. Grotevent, I. Shorubalko, S. C. Boehme and M. V. Kovalenko, Hybrid 0D Antimony Halides as Air-Stable Luminophores for High-Spatial-Resolution Remote Thermography, *Adv. Mater.*, 2021, **33**, e2007355.

49 H. Liu, T. B. Shonde, F. Gonzalez, O. J. Olasupo, S. J. Lee, D. Luong, X. S. Lin, J. S. R. V. Winfred, E. Lochner, I. Fatima, K. Hanson and B. W. Ma, Efficient Red Light Emitting Diodes Based on a Zero-Dimensional Organic Antimony Halide Hybrid, *Adv. Mater.*, 2023, **35**, e2209417.

50 N. Berova, L. Di Bari and G. Pescitelli, Application of Electronic Circular Dichroism In Configurational And Conformational Analysis of Organic Compounds, *Chem. Soc. Rev.*, 2007, **36**, 914–931.

51 F. S. Richardson and J. P. Riehl, Circularly Polarized Luminescence Spectroscopy, *Chem. Rev.*, 1977, **77**, 773–792.

52 J. A. Alonso, M. J. Martínez-Lope, M. T. Casais and M. T. Fernández-Díaz, Evolution of the Jahn–Teller Distortion of MnO_6 Octahedra in $RMnO_3$ Perovskites (R = Pr, Nd, Dy, Tb, Ho, Er, Y): A Neutron Diffraction Study, *Inorg. Chem.*, 2000, **39**, 917–923.

53 M. W. Lufaso and P. M. Woodward, Jahn-Teller Distortions, Cation Ordering and Octahedral Tilting in Perovskites, *Acta Crystallogr., Sect. B: Struct. Sci.*, 2004, **60**, 10–20.

54 Y. Y. Jing, Y. Liu, X. X. Jiang, M. S. Molokeev, Z. S. Lin and Z. G. Xia, Sb^{3+} Dopant and Halogen Substitution Triggered Highly Efficient and Tunable Emission in Lead-Free Metal Halide Single Crystals, *Chem. Mater.*, 2020, **32**, 5327–5334.